Soft Matter

PAPER

View Article Online
View Journal | View Issue

Cite this: *Soft Matter*, 2024, **20**, 4964

The peak viscosity of decaying foam with natural drainage and coarsening

Wei Yu †*[a] and Jack H. Y. Lo †*[ab]

Studying the change in foam viscosity during foam decay, a spontaneous and inevitable process, is of fundamental and practical interest across many applications, ranging from the froth in a cup of coffee to the carbon sequestration in deep geological reservoirs. However, standard rheological measurements impose several experimental constraints, such as the narrow sample confinement and the long initial setup time, interfering with the natural conditions for foam decay. Here, we perform fast and *in situ* measurements on decaying foam immediately after its generation in a wide column, measuring the viscosity by vibrational probes and measuring the foam structure by optical imaging. We successfully capture the changes during the transition from the drainage-dominated stage to the coarsening-dominated stage. The viscosity reaches its maximum at the crossover point, elucidating the competing effects of drainage and coarsening. The viscosity peaks magnitude and position are influenced by the gas solubility and diffusion coefficient. The phenomena are quantitatively explained by the film-shearing model. Our findings provide the foundation for enhancing foam stability and performance, improving the efficiency of foam-based applications.

Received 26th April 2024,
Accepted 5th June 2024

DOI: 10.1039/d4sm00498a

rsc.li/soft-matter-journal

1 Introduction

Foam, or liquid foam, is a colloidal system in which gas bubbles are enclosed by liquid. The viscosity of foam is usually several magnitudes higher than that of the constituent liquid and gas phase. This interesting property not only affects the texture of coffee and shaving cream in our daily life, but also makes foam crucial in many industrial applications, such as carbon sequestration, enhanced oil recovery, and the processing of food and cosmetics.[1–5] However, foams are thermodynamically unstable, and their structure changes over time, affecting their thermal, optical, and mechanical properties, including the foam viscosity.[6–8] The change in foam properties over time is known as foam decay or foam aging. Foam decay is a spontaneous and arguably inevitable process. Therefore, studying the change in foam viscosity during foam decay is of fundamental and practical interest.

The structure of foam decays spontaneously as soon as it is created. It is a combined result of drainage, coarsening, and coalescence.[9,10] Specifically, in this context, drainage refers to the flow of liquid through the Plateau borders and nodes induced by gravity and the capillary pressure.[11,12] Drainage reduces the liquid fraction in the foam and reduces the thickness of the liquid films between bubbles. Coarsening refers to the diffusive exchange of gas between bubbles driven by the curvature differences between adjacent foam films.[13–15] Coalescence refers to the rupture of the foam films,[16,17] but coalescence is rare in surfactant-stabilized foams.[18,19] Both coarsening and coalescence increase the average bubble size. Drainage and coarsening in foam are coupled, with faster coarsening leading to faster drainage.[19] Despite this coupling, one of these effects can be more prominent than the other. We refer to these scenarios as either a drainage-dominated stage or coarsening-dominated stage. In both stages, both drainage and coarsening contribute to the foam decay, though to varying degrees.

Foam viscosity is defined as the ratio of the loss modulus to the oscillation frequency in rheology. There are two different types of theoretical models to describe the foam viscosity: the film-stretching model or the film-shearing model. In the film-stretching model, the viscous dissipation is mainly contributed by the flow in the transition region between the Plateau border and the film.[20–22] On the other hand, in the film-shearing model, the viscous dissipation is mainly contributed by the shearing flow in the film. The bubble surfaces are assumed to be immobile due to the high surface dilatational viscosity and surface Marangoni stress. The film-shearing model suggests that the shear stress, and hence the viscosity, is inversely proportional to the film thickness.[22–25] The film-shearing model has been verified experimentally on ageless/non-decaying foam

[a] *Center for Integrative Petroleum Research (CIPR), College of Petroleum Engineering and Geosciences, King Fahd University of Petroleum and Minerals, Dhahran 31261, Saudi Arabia. E-mail: wei.yu@kfupm.edu.sa*
[b] *Division of Physical Sciences and Engineering, King Abdullah University of Science and Technology (KAUST), Thuwal 23955-6900, Saudi Arabia. E-mail: hauyung.lo@kaust.edu.sa*
† These authors contributed equally to this work.

with constant bubble size,[22,23] here we will apply this model on decaying foam.

Experimentally, the rheology properties of foam have been frequently studied by using a rheometer.[8,22,23,26–31] However, this method faces several challenges in studying foam decay. Using rheometers, foams are confined in a narrow gap ($\sim$1 mm thick typically) between the rotor and the sample container. This confinement may affect the foam decay process, including the drainage and the coarsening. Typically, in contrast, the stability of a decaying foam is measured in a much wider column, without such narrow confinement (*e.g.* ASTM D1173 and ISO 696). Second, rheometer measurements take a considerable amount of time. The period of time between loading the sample and completing the first measurement is long compared to the early dynamics of foam decay. To address the above technical challenges about speed and confinement, we have recently proposed the use of a vibrational viscometer to measure the foam viscosity at fixed shear rate and amplitude.[32] Our experimental setup allows foam to decay with free drainage and coarsening in a wide open space. We describe this condition as the natural decay or aging of foam, in contrast to setups that feature forced drainage, fixed bubble size, and a narrow gap.

In this work, we investigate the change in foam viscosity of naturally decay foam. To achieve this, we measure the viscosity by vibrational probes and measure the foam structure by optical imaging. The measurement starts immediately after the foam is generated in a foam column. The fast and *in situ* measurement allows us to capture the transition from the drainage-dominated stage to the coarsening-dominated stage. As a result of the competition between drainage and coarsening, the viscosity peaks at a certain time. In contrast, previous studies observed a monotonic decrease in viscosity during foam decay, aligning with the later stage of our measurements.[31,33] We compare the measured viscosity and foam structures with the film-shearing model.[22,23] We elucidate the relation between the foams effective diffusion coefficient and the characteristics of the viscosity peak, including its height and position, by investigating foams that are generated by different gases.

2 Experimental methods

Foams used in this work were prepared with 10 mM sodium dodecylsulfate (SDS, Sigma Aldrich), deionized water (DI, Milli-Q, Sigma-Aldrich), high-purity nitrogen (N_2, 99.9%), carbon dioxide (CO_2, 99.9%), and sulfur hexafluoride (SF_6, 99.9%) (Saudi Industrial Gas Company Ltd).

Foams are generated and measured in the same setup as illustrated in Fig. 1. The foam is generated by flowing a gas through the porous glass frit into a surfactant solution in a glass column. The glass column has an inner diameter D of 68 mm and a height T of 60 mm. Between the cylindrical part and the conical section of the foam column is a sintered glass frit with a pore size of 10–15 μm. The conical section ensured a uniform distribution of the gas through the frit. The gas flow rates are controlled by two mass flow meters (GE50A, MKS Instruments). A valve and a gas mixer are set between the glass column and the mass flow meters. The valve is used to avoid the backflow of the surfactant solution. The gas mixer is used for mixing two gas streams (*e.g.*, N_2 and CO_2) in some experiments.

The initial foam column height of 60 mm is selected to ensure that the foam can be quickly produced within 20 s by our experimental setup. This ensures that the foam production time is negligible when compared to the foam decay time. Because we measure the viscosity of the top layer of the foam,

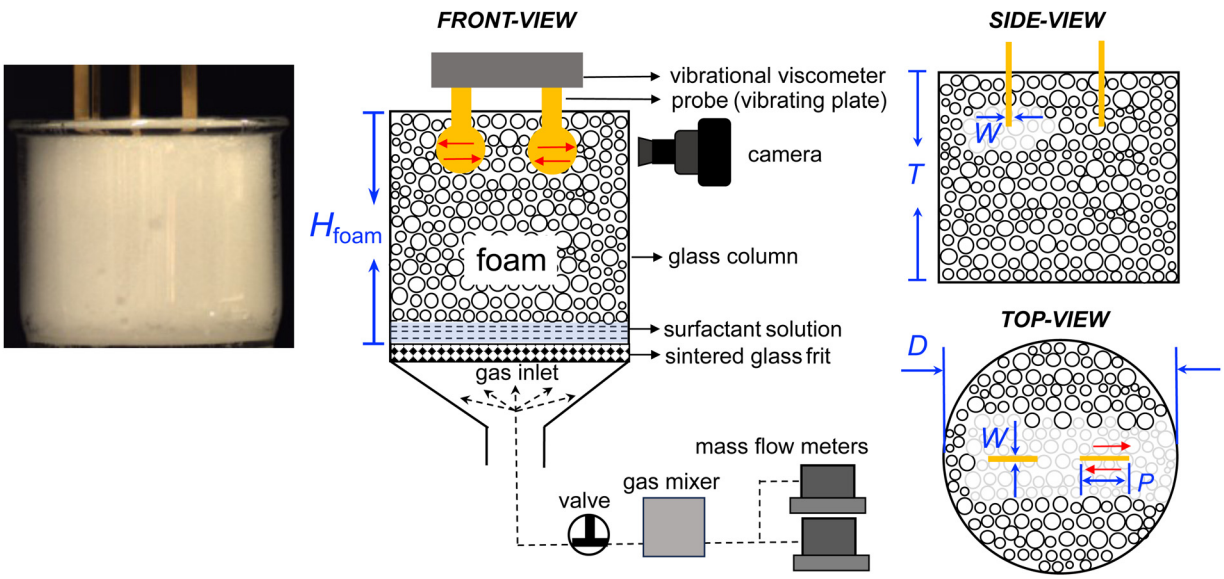

Fig. 1 Experimental setup for foam generation and *in situ* measurements. The foam is generated by flowing a gas through the porous glass frit into a surfactant solution in a glass column. The glass column has a height of T = 60 mm and an inner diameter of D = 68 mm. A photo of the setup and foam column is shown. The foam viscosity is measured immediately after the generation of foam by a tuning-fork vibrational viscometer. The two vibrating plates oscillating parallel to their surfaces (indicated by red arrows) at a frequency of 30 Hz and an amplitude of 400 μm. The vibrating plates have a diameter of P = 13 mm and a thickness of W = 0.5 mm. The foam height H_{foam} and foam structures are measured simultaneously by a high-resolution camera.

the column height does not affect our measurement. If measurements were taken deeper within the foam, the depth will affect the evolution of liquid fraction and thus the viscosity. In that case, the liquid fraction would initially remain constant for a period of time before starting to decrease.

The foam viscosity is measured immediately after the generation of foam in the same setup as illustrated in Fig. 1. The foam viscosity is measured by a tuning-fork vibrational viscometer (SV-10, A&D Company).[32,34] In this setup, two thin plates are immersed in the foam and the plates vibrate sinusoidally at a fixed frequency of 30 Hz and a fixed amplitude of 400 μm. For a sample with a viscosity of ~200 cP, the penetration depth δ is 4.6 mm and the shear strain γ is ~9%.[32] The vibrating plates have a diameter P of 13 mm and a thickness W of 0.5 mm. We estimate that about 1800–17 000 bubbles are in contact with the vibrating plates, depending on the bubble sizes at different time. In a previous study,[32] we have verified the reliability of the vibrational viscometer by comparing its measurement results with those of a rheometer (MCR 702, Anton Paar). Moreover, by conducting the intermittent on–off test, we have demonstrated that the vibration of the probes did not disturb the foam decay.

The foam structures, including the sizes of bubbles, plateau borders, and nodes, are measured simultaneously by a high-resolution camera as shown in Fig. 1 and 2. The foam height H_{foam} is also measured simultaneously by a camera as shown in Fig. 1. The interfacial tension between the surfactant solution and the gases is measured by the pendant drop method (theta flex optical tensiometer, Biolin Scientific).

The experimental procedures are outlined as follows. At the beginning of each experiment, the glass column and frit were thoroughly rinsed with isopropanol and DI water. The vibrating plates of the viscometer were hung at a pre-defined height in the glass column (Fig. 1). We first flushed the glass column with the tested gas at a constant flow rate of 100 mL min^{-1} for 3 min. Then, we increased the gas flow rate to 200 mL min^{-1} and quickly poured 50 mL of the surfactant solution into the glass column. The surfactant solution started foaming as the gas flew through the porous frit. The bubbles began rising from the bottom of the glass column and accumulated to form foams. The gas continued flowing for around 30 s until the foam fully covered the sensor plates. Lastly, we swiftly stopped the gas injection, closed the valve, and started the viscosity measurement.

To capture the change in foam viscosity in a timely manner, the viscometer was turned on before gas bubbles reached the sensor plates. This method is an improvement over our previous method, where the measurements were not quick enough to capture the initial dynamics of foam decay.[32] We define time t = 0 as the moment when the foam reached the preset height and gas injection was stopped. The schematic illustration and photos of a typical measurement in the initial and final states are shown in Fig. 1. All experiments were performed at room temperature (22 ± 1 °C) and ambient pressure.

3 Results and discussion

The measured viscosity of a decay foam at different time is shown in Fig. 3. The foam is made of SDS aqueous solution and N_2 gas. The foam is freshly produced *in situ* at the time t = 0. We observe that the foam viscosity increases during stage I ($t < t_{peak}$) and decreases during stage II ($t > t_{peak}$). The viscosity reaches its maximum at the crossover point ($t = t_{peak}$). To the best of our knowledge, this viscosity peak has not been studied before.

The change in viscosity is correlated to the change in foam structures. The foam structures, including the sizes of bubbles,

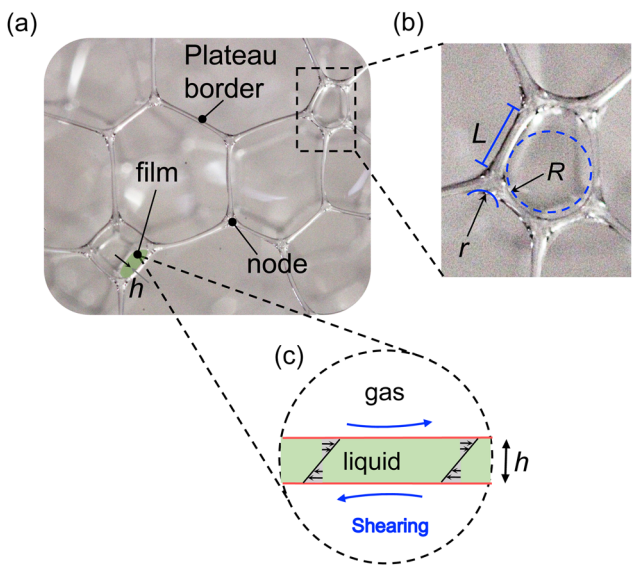

Fig. 2 Foam structures are measured simultaneously by a high-resolution camera. (a) The liquid films, Plateau borders, and nodes are illustrated in the photo. (b) The effective bubble radius, R, the node radius, r, and the Plateau border length, L, are measured. (c) Schematic illustration of a shearing liquid film with thickness h.

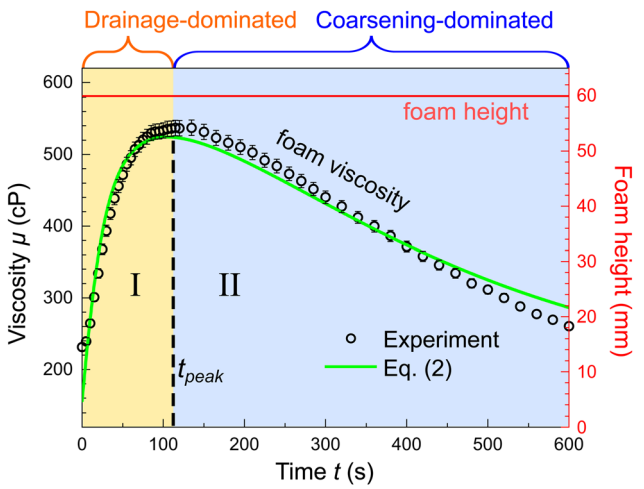

Fig. 3 Peak viscosity of a decaying foam. The foam viscosity (black circles) increases during stage I ($t < t_{peak}$) and decreases during Stage II ($t > t_{peak}$). The viscosity reaches its maximum at the crossover point ($t = t_{peak}$). We find that stage I is the drainage-dominated stage, and the stage II is the coarsening-dominated stage. The green line represents eqn (2) of the film-shearing model, it agrees with the experimental data. The constant foam height indicates that coalescence is negligible. The foam is made of SDS and N_2.

plateau borders, and nodes, are measured simultaneously with the viscosity. Some examples of the microscopic images are given in Fig. 4(a). The images used in the analysis are much larger than the portion of images shown here. We measured the bubble radius R, Plateau border length L, and node radius r from the images, as illustrated in Fig. 2. We sampled $\sim$ 100 bubbles at each time frame and calculated the average values of R, L, and r. The sampled foams are located at the same height as the sensor plates of the viscometer, ensuring that the measured foam structures can be correlated with the measured viscosity. Moreover, we observed that the bubbles did not coalesce, consistent with the previous studies.[18,19]

We also measured the foam height, H_{foam}, as shown in Fig. 3. The foam height measures the height of the air/foam interface at the top of the foam column, as defined in Fig. 1. It does not reflect the change in height of the liquid/foam interface at the bottom of the foam column due to drainage. The measured foam height remains constant throughout the duration of the experiment considered in this study. The constant foam height means that the total volume of the gas bubbles in the foam is constant. This implies that there is no film rupture at the top of the foam that would release gas bubbles into the atmosphere. Because the film at the top of the foam is the thinnest when compared to that in the other region of the foam, the constant foam height suggests that coalescence is negligible. This echoes the observations of microscopic images above.

The measurement of foam structures clarifies the underlying mechanism behind the peak viscosity, as shown in Fig. 4.

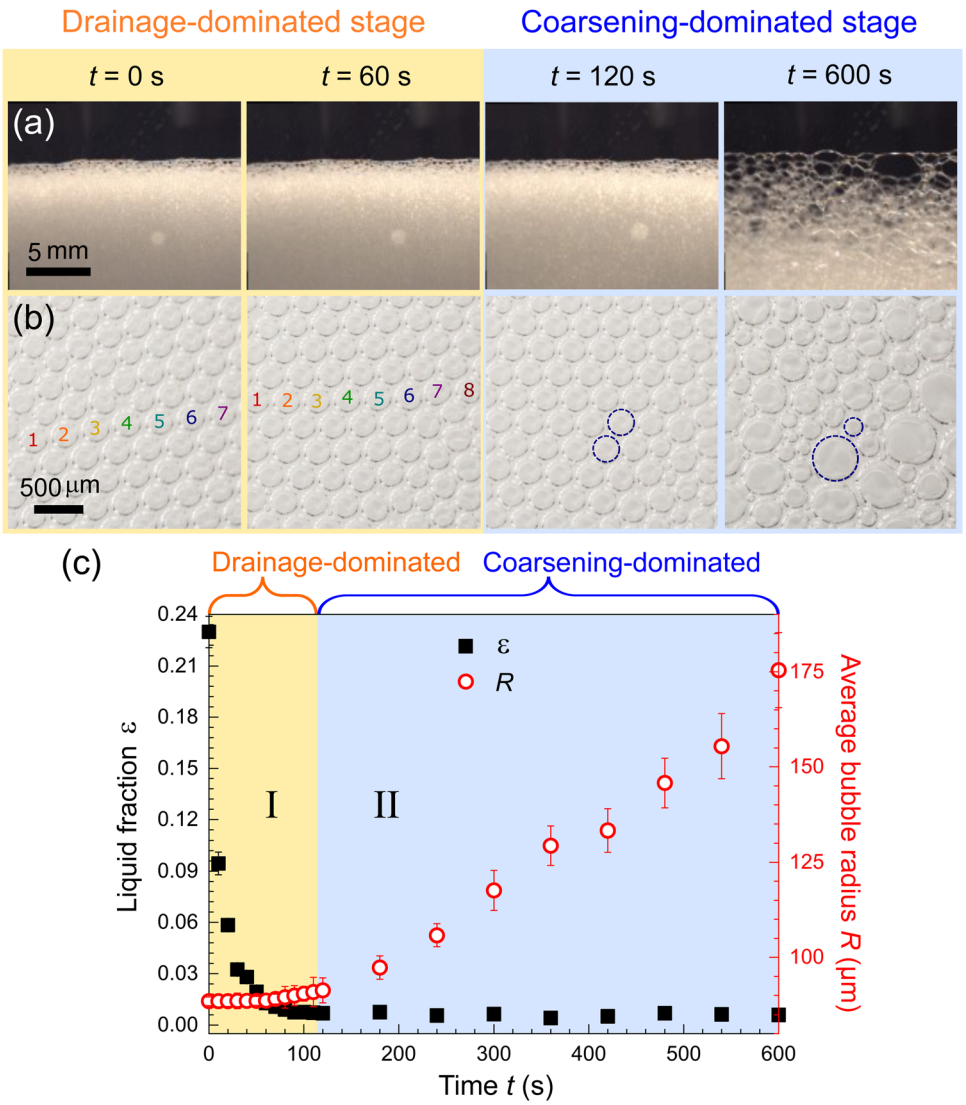

Fig. 4 The measurement of foam structures clarifies the underlying mechanism behind the peak viscosity. (a) and (b) Examples of captured photos and microscopic images of foam at different time. The number density of bubbles increases due to drainage during stage I, and the bubble radius varies due to coarsening during stage II. Larger images with more bubbles are used in the subsequent measurements. (c) The measured liquid fraction ε and average bubble radius R at different time. The liquid fraction is calculated from the Plateau boarder length and node radius by eqn (1). The standard deviation of radius are represented by the error bars. The data show that stage I is the drainage-dominated stage and stage II is the coarsening-dominated stage. The measured data is used to plot eqn (2) in the Fig. 3 (green line in Fig. 3).

We identify stage I as the drainage-dominated stage and stage II as the coarsening-dominated stage by observing the microscopic images, as shown in Fig. 4(b). It is obvious that the number density of bubbles increases due to drainage during stage I, and the bubble radius varies due to coarsening during stage II. The liquid fraction and the average bubble radius are measured at different time, as shown in Fig. 4(c). The average bubble radius $R(t)$ is an average of $\sim$ 100 bubbles. The liquid fraction $\varepsilon(t)$ is calculated by

$$\varepsilon = 0.171\left(\frac{r}{L}\right)^2 + 0.2\left(\frac{r}{L}\right)^3 \quad (1)$$

where r and L are the average values of the node radius and the Plateau border length, respectively.[11] A plot of the liquid fraction ε and the average bubble radius R at different time t is shown in Fig. 4(c). For the ease of comparison, we have divided the plot into two regions, based on the peak time t_{peak} identified in the previous plot of viscosity (Fig. 3). In stage I ($t < t_{peak}$), ε decreases rapidly from 0.230 to 0.006, while R increases slowly. In stage II ($t > t_{peak}$), in contrast, the change in ε is very small and negligible, while the R increases faster from 91 to 175 μm. Therefore, the change in viscosity in stage I is attributed to the drainage, and that in stage II is attributed to the coarsening.

We find that the existence of the viscosity peak agrees with the prediction of the film-shearing model by considering the measured $R(t)$ and $\varepsilon(t)$.[22–24] The film-shearing model shows that the shear stress is the product of the Laplace pressure and the shear across foam films, which is inversely proportional to film thickness. Accordingly, the foam viscosity can be expressed as

$$\mu(t) \propto \frac{\sigma}{\dot{\gamma}R(t)h(t)} = \frac{\sigma}{\dot{\gamma}R(t)}\frac{g}{1+h'\varepsilon(t)} \quad (2)$$

where σ = 35 mN m^{-1} is the interfacial tension, $\dot{\gamma} = 16^{-1}$ is the shear rate of the measurement, $R(t)$ is the bubble radius, $h(t) \propto 1 + h'\varepsilon(t)$ is the film thickness expressed by a first-order approximation, $\varepsilon(t)$ is the liquid fraction, h' and g are dimensionless parameters that will be deduced by curve fittings. By considering the measured $R(t)$ and $\varepsilon(t)$, we find that eqn (2) agrees with the data very well, as shown in Fig. 3, with the best fits g = 0.024 and h' = 12. In particular, the theoretical model successfully reproduces the viscosity peak, which has not been reported before.

The film-shearing model also provides a more precise explanation for the underlying mechanism of the viscosity changes. As shown by eqn (2), drainage and coarsening have opposing effects on foam viscosity. In the initial stage, when drainage is more significant than coarsening, the foam viscosity increases because the gap between bubbles decreases. In the second stage, when coarsening is more significant than drainage, the foam viscosity increases because the bubble size increases. The viscosity attains its maximum value when the effects of the drainage and coarsening balance each other. According to eqn (2), it happens when $(dR/dt)/R = -(dh/dt)/h$.

The film-shearing model is originally developed for monodisperse foams such that all constant bubble radius.[22–24] Here, we have applied it to polydisperse foams by using the average bubble radius in substitution and showing a satisfying outcome. Practically, a natural aging foam must be polydisperse due to the coarsening. Similarly, the film-shearing model has been verified experimentally on non-decaying foam (ageless foam),[22,23] here we have applied the model on decaying foam.

We further clarify the role of drainage and coarsening by a pulsed perfusion test.[22,23] We add surfactant solution at intervals of 100 s from the top of the foam (see the inset of Fig. 5). In each cycle of perfusion (indicated by the labels #1 to #5), first, the foam viscosity decreases rapidly due to the sudden increase in the liquid fraction. Next, the viscosity increases and reaches a local maximum due to drainage. Finally, the viscosity decreases due to coarsening. The local maxima are decreasing in each successive perfusion due to the irreversible decrease in average bubble size. This perfusion test complements that of Soller *et al.*,[22,23] where the average bubble size was maintained at a constant value. In their experiments, consequently, the viscosity peaks were absent.

The characteristics of the viscosity peak, including its magnitude and position, are different in different foams. We prepared foams made of different types of gas, including N_2, SF_6, and CO_2–N_2 mixtures with varying mixing ratios. The measured viscosity $\mu(t)$, liquid fraction $\varepsilon(t)$, and average bubble radius $R(t)$ over time t as shown in Fig. 6(a–c). The corresponding values of h' and g are listed in Table (1). It has been shown that the parameter g depends on the capillary number of the fluid.[22] In our experiments, the capillary number remains unchanged since we only vary the gas, while both the strain rate and the fluid remain the same. Therefore, the obtained values of g are close to each other.

Comparing the measured viscosity of foam generated by different gases, we find that the CO_2–N_2 mixtures have lower peak heights than that of pure N_2, which, in turn, is lower than

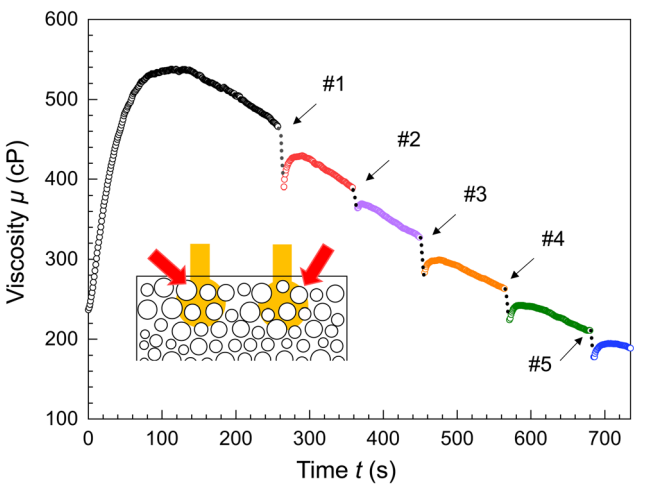

Fig. 5 The pulsed perfusion test further clarifies the role of drainage and coarsening. In the pulsed perfusion test, surfactant solution was injected at the top of the foam intermittently, as indicated by labels #1 to #5 and illustrated in the inset. The injected volume is 1 mL (#1), 0.2 mL (#2) and 0.5mL (#3 to #5). The viscosity reaches its local maximum in each cycle of perfusion. The local maxima are decreasing in each successive perfusion due to the irreversible decrease in average bubble size.

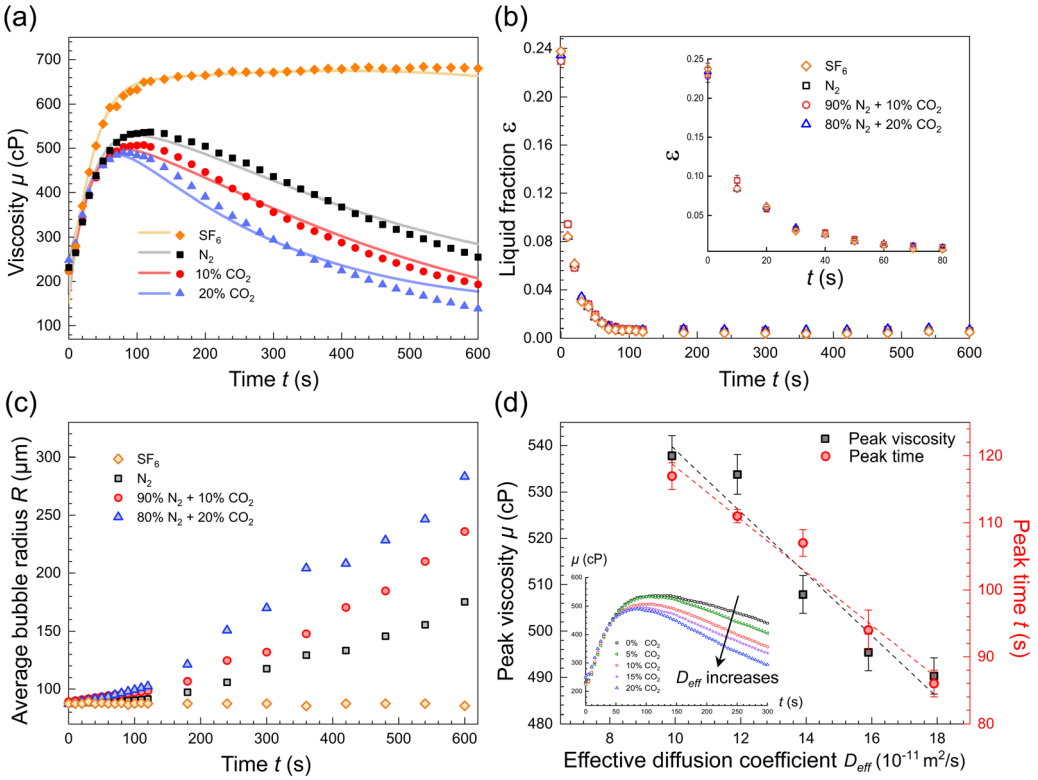

Fig. 6 The differences in viscosity peaks for foam generated by different gases. (a) Experimental data (dots) and eqn (2) (lines) of foam viscosity *versus* time. The foams are generated by SF_6 (orange), N_2 (black), 10% CO_2 + 90% N_2 (red), and 20% CO_2 + 80% N_2 (blue). (b, c) Comparing the liquid fraction and average bubble radius across different gases at different time. The trend in liquid faction is almost the same, while the trend in bubble radius varies significantly. The inset in (b) is the zoom-in of the data in the initial 80 seconds. (d) The peak viscosity and peak time decrease with increasing effective diffusion coefficient D_{eff}, as indicated by the dashed lines. The physical constants used to calculate D_{eff} are listed in Table (2). The inset in (d) show the viscosity data of the tested foams corresponding to the five different D_{eff}.

Table 1 Best-fit values of g and h' in eqn (2) for the data in Fig. 6(a)

Gas	g ($\times 10^{-3}$)	h'
SF_6	27.7 ± 0.3	15 ± 1
N_2	24.0 ± 0.4	12 ± 1
90% N_2, 10% CO_2	23.8 ± 0.4	11 ± 1
80% N_2, 20% CO_2	23.7 ± 0.6	11 ± 1

Table 2 Henrys law constant He, diffusion coefficient in water D, and the calculated effective diffusion coefficient D_{eff} for SF_6, N_2, CO_2 and CO_2-N_2 mixtures

Gas	He[35,36] (mol m^{-3} Pa^{-1})	D[37,38] (m^2 s^{-1})	$D_{eff} = kD$He (m^2 s^{-1})
SF_6	2.4×10^{-6}	9.8×10^{-10}	0.17×10^{-10}
N_2	6.4×10^{-6}	19×10^{-10}	0.96×10^{-10}
CO_2	3.4×10^{-6}	18×10^{-10}	44×10^{-10}
80% N_2, 20% CO_2	7.3×10^{-5}	19×10^{-10}	9.4×10^{-10}

that of SF_6. Similar trends are also observed for the position of the peak (*i.e.* peak time). The CO_2–N_2 mixtures reach the peak in shorter times than N_2 and SF_6. The required time for SF_6 to reach the peak is so long that it exceeds the total duration of our experiment. The observed results hint that the height and position of the peak depend on the gas solubility and diffusion coefficient in water, which are listed in Table (2). We have carried out the following analysis to provide a more detailed explanation.

To explain the difference in the viscosity peak among different foams, we compare the drainage rate and coarsening rate of the foams. Here, we define the drainage rate as the rate of change in liquid fraction over time. We found that the liquid fraction decreases at almost the same rate for different gases, as shown in Fig. 6(b). Therefore, the drainage rate is independent of the gas types. We define the coarsening rate as the rate of change in average bubble radius over time. The average bubble radius of CO_2–N_2 mixtures increases more rapidly than that of N_2, and the rate of N_2, in turn, is faster than that of SF_6, as shown in Fig. 6(c). Therefore, in contrast to the drainage rate, the coarsening rate varies significantly among different gas types.

In principle, the drainage and the coarsening in foam are coupled, such that faster coarsening would lead to faster drainage.[19] However, in our system, it seems that the drainage rate is unaffected by the difference in coarsening rate. This is probably because the initial drainage rate is significantly faster than the coarsening rate. By the time that coarsening effect become prominent, the liquid fraction and drainage rate is very low, as shown in Fig. 4(c). Therefore, the coupling effect is not significant for the viscosity peak.

By knowing that the drainage rates are practically the same, but the coarsening rates are different, we can explain the trend of the viscosity peak. As described by the film-shearing model and eqn (2), the viscosity peak results from the competition of drainage and coarsening, which occurs at $(dR/dt)/R = -(dh/dt)/h$, where the film thickness h is a function of liquid fraction. The drainage affects right hand side of the equation, which is practically invariant to the gas type. The coarsening affects the left hand side of the equation, which depends on the physical properties of the gas.

To understand how the physical properties of the gas affect the coarsening and hence the viscosity peak, we repeated the experiments systematically with foam made of different ratios of CO_2–N_2 mixtures, ranging from 0 to 20% of CO_2, with an interval of 5%. The measured viscosity is shown in the inset of Fig. 6(d). It is well known that the coarsening rate in a foam depends on the gas solubility and diffusion coefficient.[19,39,40] Specifically, the rate of change in bubble size (edge length) is proportional to the effective diffusion coefficient given by[19]

$$D_{\text{eff}} = kD\text{He} \quad (3)$$

where D is the diffusion coefficient and He is Henrys law constant. The constant $k = 7.14 \times 10^3$ m^3 Pa mol^{-1} is calculated under the assumption of ideal gas in dry foam, it is a product of several other constants and the explicit formula can be found in the references cited here.[19,39,40] Although the assumption of dry foam is invalid initially due to the high liquid fraction, it becomes acceptable when the viscosity approaches its maximum, as the liquid fraction becomes low ($\varepsilon < 0.01$) from this time onwards, as shown in Fig. 4(c) and 6(b). The values of D, He, and D_{eff} of the tested gases are listed in Table (2). For the gas mixtures, D and He are obtained using the partition law. The calculated values of D_{eff} of the SF_6, N_2, and CO_2(20%)–N_2 mixture are 0.2, 1, and 9.4, respectively. The measured height (peak viscosity) and position (peak time) of the peaks are plotted with respect to their effective diffusion coefficient D_{eff}, as shown in Fig. 6(d). As the effective diffusion coefficient increases, both the peak viscosity and the peak time decrease. The results verify that the variation of the peaks among different foams arises from the variation in effective diffusion coefficient.

Among the different gas types, the variation in diffusion coefficient are much smaller than that in solubility. For example, CO_2 is two orders of magnitudes more soluble than SF_6, but its diffusion coefficient is only twice as large as that of SF_6. Therefore, for the examples demonstrated in this study, the variation of the peaks is mainly due to the variation in solubility. The potential for varying the diffusion coefficient has yet to be explored.

4 Conclusions

In conclusion, our experiments have successfully captured the changes in viscosity and foam structure during the transition from the drainage dominated stage to the coarsening dominated stage. In the drainage-dominated stage, the foam viscosity increases over time. Conversely, in the coarsening-dominated stage, the foam viscosity decreases over time. The viscosity reaches its maximum at the crossover point. We find that the existence of the viscosity peak agrees with the prediction of the film-shearing model by considering the changes in foam structures, including the liquid fraction and the average bubble size. We find that coalescence does not occur in our system as expected. We also find that the characteristics of the viscosity peak, including its magnitude and position, depend on the physical properties of the gas in the foam. The choice of gas affects the coarsening rate, while the drainage rate is unaffected. The coupling effect between the drainage and the coarsening is not significant for the viscosity peak. The magnitude and position of the viscosity peak decrease as the effective diffusion coefficient increases.

Besides understanding the viscosity peak, our results suggest that the film-shearing model, which was originally developed for monodisperse foams,[22–24] is also applicable to polydisperse foams. This is valuable because, naturally, a decaying foam would be polydisperse due to the coarsening. Furthermore, previously, the film-shearing model has been verified experimentally on non-decaying foam (ageless foam),[22,23] while here we have verified it on decaying foam.

We anticipate generalizing our findings to more complicated scenarios. For example, we notice that viscosity peaks also appear in core flooding experiments that use foam to displace crude oil.[41] In this scenario, the primary challenge in testing the mechanism lies in the difficulty of measuring the foam structures within the rock. Our findings suggest potential strategies for enhancing the performance and stability of foam by considering the competition between drainage and coarsening. Our work may shed light on studying the stabilization mechanisms of foam enhancers, such as polymer solutions,[42–44] emulsions,[33,45] and functionalized nanoparticles.[46–51]

Author contributions

W. Y. and J. H. Y. L. contributed equally to this work.

Data availability

The data supporting this article have been included in the manuscript.

Conflicts of interest

There are no conflicts to declare.

Acknowledgements

We thank Mazen Kanj for his advice in the experiment design, Zhengwei Pan and Yafei Chen for their help in experiments and fruitful discussion, Jafar Sadeq Al Hamad for his assistance in using the rheometer, Howard A. Stone and Yuan Liu for their suggestions on the manuscript. J. H. Y. L. acknowledges financial

support from King Abdullah University of Science and Technology under grant BAS/1/1352-01-01 and Sigurdur Thoroddsen.

Notes and references

1 B. S. Murray, *Curr. Opin. Colloid Interface Sci.*, 2020, **50**, 101394.
2 C. Hill and J. Eastoe, *Adv. Colloid Interface Sci.*, 2017, **247**, 496–513.
3 W. Yu and M. Y. Kanj, *J. Pet. Sci. Eng.*, 2022, **208**, 109698.
4 W. Wanniarachchi, P. Ranjith and M. Perera, *Environ. Earth Sci.*, 2017, **76**, 1–15.
5 Y. Luo, M. Chen, D. Liu, Y. Jin, M. Du and J. Hou, *Pet. Sci. Technol.*, 2012, **30**, 1747–1754.
6 Y. Lu, S. Shi, H. Wang, Z. Tian, Q. Ye and H. Niu, *Int. J. Heat Mass Transfer*, 2019, **131**, 594–603.
7 M. U. Vera, A. Saint-Jalmes and D. J. Durian, *Appl. Opt.*, 2001, **40**, 4210–4214.
8 S. Cohen-Addad and R. Höhler, *Curr. Opin. Colloid Interface Sci.*, 2014, **19**, 536–548.
9 K. Małysa, *Adv. Colloid Interface Sci.*, 1992, **40**, 37–83.
10 O. Pitois, S. Cohen-Addad and R. Höhler, *Annu. Rev. Fluid Mech.*, 2013, **45**, 241.
11 S. A. Koehler, S. Hilgenfeldt and H. A. Stone, *Langmuir*, 2000, **16**, 6327–6341.
12 S. Sett, S. Sinha-Ray and A. Yarin, *Langmuir*, 2013, **29**, 4934–4947.
13 H. Flyvbjerg, *Phys. Rev. E*, 1993, **47**, 4037.
14 A. Saint-Jalmes, *Soft Matter*, 2006, **2**, 836–849.
15 S. Magrabi, B. Dlugogorski and G. Jameson, *Chem. Eng. Sci.*, 1999, **54**, 4007–4022.
16 D. Langevin, *Curr. Opin. Colloid Interface Sci.*, 2019, **44**, 23–31.
17 A. Bhakta and E. Ruckenstein, *Adv. Colloid Interface Sci.*, 1997, **70**, 1–124.
18 S. A. Koehler, S. Hilgenfeldt, E. R. Weeks and H. A. Stone, *Phys. Rev. E*, 2002, **66**, 040601.
19 S. Hilgenfeldt, S. A. Koehler and H. A. Stone, *Phys. Rev. Lett.*, 2001, **86**, 4704.
20 H. Princen and A. Kiss, *J. Colloid Interface Sci.*, 1989, **128**, 176–187.
21 L. Schwartz and H. Princen, *J. Colloid Interface Sci.*, 1987, **118**, 201–211.
22 R. Soller and S. A. Koehler, *Phys. Rev. Lett.*, 2008, **100**, 208301.
23 R. Soller and S. A. Koehler, *Phys. Rev. E*, 2009, **80**, 021504.
24 D. Buzza, C.-Y. Lu and M. Cates, *J. Phys. II*, 1995, **5**, 37–52.
25 N. Denkov, S. Tcholakova, K. Golemanov, K. Ananthapadmanabhan and A. Lips, *Phys. Rev. Lett.*, 2008, **100**, 138301.
26 K. Krishan, A. Helal, R. Höhler and S. Cohen-Addad, *Phys. Rev. E*, 2010, **82**, 011405.
27 A. Gopal and D. J. Durian, *Phys. Rev. Lett.*, 2003, **91**, 188303.
28 B. Dollet and C. Raufaste, *C. R. Phys.*, 2014, **15**, 731–747.
29 S. Costa, R. Höhler and S. Cohen-Addad, *Soft Matter*, 2013, **9**, 1100–1112.
30 S. Marze, R.-M. Guillermic and A. Saint-Jalmes, *Soft Matter*, 2009, **5**, 1937–1946.
31 S. Cohen-Addad, H. Hoballah and R. Höhler, *Phys. Rev. E*, 1998, **57**, 6897.
32 W. Yu, J. H. Y. Lo and M. Y. Kanj, *Langmuir*, 2023, **39**, 14711–14717.
33 C. Guidolin, J. Mac Intyre, E. Rio, A. Puisto and A. Salonen, *Nat. Commun.*, 2023, **14**, 1125.
34 J. Woodward, *J. Acoust. Soc. Am.*, 1953, **25**, 147–151.
35 A. Penttilä, C. DellEra, P. Uusi-Kyyny and V. Alopaeus, *Fluid Phase Equilib.*, 2011, **311**, 59–66.
36 J. L. Bullister, D. P. Wisegarver and F. A. Menzia, *Deep Sea Res., Part I*, 2002, **49**, 175–187.
37 S. P. Cadogan, G. C. Maitland and J. M. Trusler, *J. Chem. Eng. Data*, 2014, **59**, 519–525.
38 D. King and E. Saltzman, *J. Geophys. Res: Oceans*, 1995, **100**, 7083–7088.
39 A. Saint-Jalmes and C. Trégouët, *Soft Matter*, 2023, **19**, 2090–2098.
40 H. Princen and S. Mason, *J. Colloid Sci.*, 1965, **20**, 353–375.
41 M. H. Alooghareh, A. Kabipour, S. M. M. Sisakht and M. Razavifar, *et al.*, *Petroleum*, 2022, **8**, 546–551.
42 T. Majeed, M. S. Kamal, X. Zhou and T. Solling, *Energy Fuels*, 2021, **35**, 5594–5612.
43 Q. Shi, B. Qin, Y. Xu, M. Hao, X. Shao and H. Zhuo, *Fuel*, 2022, **313**, 122685.
44 G. Gochev, *Curr. Opin. Colloid Interface Sci.*, 2015, **20**, 115–123.
45 R. Rafati, O. K. Oludara, A. S. Haddad and H. Hamidi, *Colloids Surf., A*, 2018, **554**, 110–121.
46 X. Chen, C. Da, D. C. Hatchell, H. Daigle, J.-R. Ordonez-Varela, C. Blondeau and K. P. Johnston, *J. Colloid Interface Sci.*, 2023, **630**, 828–843.
47 C. Da, X. Chen, J. Zhu, S. Alzobaidi, G. Garg and K. P. Johnston, *J. Colloid Interface Sci.*, 2022, **608**, 1401–1413.
48 X. Song, X. Cui, X. Su, B. Munir and D. Du, *J. Pet. Sci. Eng.*, 2022, **218**, 111065.
49 S. Li, K. Yang, Z. Li, K. Zhang and N. Jia, *Energy Fuels*, 2019, **33**, 5043–5054.
50 K. Aono, K. Ueno, S. Hamasaki, Y. Sakurai, S.-I. Yusa, Y. Nakamura and S. Fujii, *Langmuir*, 2022, **38**, 7603–7610.
51 A. Roux, A. Duchesne and M. Baudoin, *Phys. Rev. Fluids*, 2022, **7**, L011601.